

Denoising of Sphere- and $SO(3)$ -Valued Data by Relaxed Tikhonov Regularization

Robert Beinert* Jonas Bresch[†] Gabriele Steidl[‡]

May 17, 2024

Abstract

Manifold-valued signal- and image processing has received attention due to modern image acquisition techniques. Recently, a convex relaxation of the otherwise nonconvex Tikhonov-regularization for denoising circle-valued data has been proposed by Condat (2022). The circle constraints are here encoded in a series of low-dimensional, positive semi-definite matrices. Using Schur complement arguments, we show that the resulting variational model can be simplified while leading to the same solution. The simplified model can be generalized to higher dimensional spheres and to $SO(3)$ -valued data, where we rely on the quaternion representation of the latter. Standard algorithms from convex analysis can be applied to solve the resulting convex minimization problem. As proof-of-the-concept, we use the alternating direction method of multipliers to demonstrate the denoising behavior of the proposed method. In a series of experiments, we demonstrate the numerical convergence of the signal- or image values to the underlying manifold.

Keywords— Denoising of manifold-valued data, sphere- and $SO(3)$ -valued data, signal and image processing on graphs, Tikhonov regularization, convex relaxation.

2020 AMS Mathematics Subject Classification — 94A08, 94A12, 65J22, 90C22, 90C25

1 Introduction

With the emergence of modern acquisition techniques which produce manifold-valued signals and images, research in this field focuses new challenges. Circle-valued data appear in interferometric synthetic aperture radar [14, 20, 36], color image restoration in HSV or LCh spaces [31], Magnetic Resonance Imaging [28], biology [39], psychology [19] and various other applications involving the phase of Fourier transformed data for instance. Signals and images with values on the 2-sphere play a role when dealing with 3d directional information [1, 27, 41] or in the processing of color images in the chromaticity-brightness setting [5, 34, 35]. The rotation group $SO(3)$ was considered in tracking and motion analysis

*R. Beinert is with the Institute of Mathematics, Technische Universität Berlin, Straße des 17. Juni 136, 10623 Berlin, Germany.

[†]J. Bresch is with the Institute of Mathematics, Technische Universität Berlin, Straße des 17. Juni 136, 10623 Berlin, Germany.

[‡]G. Steidl is with the Institute of Mathematics, Technische Universität Berlin, Straße des 17. Juni 136, 10623 Berlin, Germany.

and in the analysis of electron back-scatter diffraction data (EBSD) [3, 4, 22]. Quaternion-valued data also arises in color image restoration, concerning the hue, saturation, and value color space [26].

The denoising of circle- and sphere-valued data was addressed by several methods as lifting procedures [18, 30, 40], variational approaches with total variation-like (TV-like) regularizers [2, 42] and half-quadratic minimization models like the iteratively re-weighted least squares method [8, 23]. These methods either enlarge the dimension of the problem drastically, especially for lifting methods, have restricted convergence guarantees, or rely on data on Hadamard manifolds, which spheres are not. There are few stochastic approaches in manifold-valued data processing as the work of Penneç’s group, see for instance [29, 33], where a patch-based approach via a minimum mean square estimation (MMSE) model on the respective manifold is applied. For an overview, we also refer to [9]. For denoising matrix-manifolds and matrix-valued images, which become a mayor part of computer vision, image processing and motion analysis, the rotation group $SO(n)$, the special-euclidean group $SE(n)$ and the symmetric positive definite matrices $SPD(n)$ are of mayor interest. For instance, [37, 38] consider a TV regularizer on the different Lie-groups for rigid 3D motions, minimizing the irregularity of the motion field.

In this paper, we focus exclusively on the important simple variational model with quadratic Tikhonov regularization that penalizes the squared differences of adjacent values on a graph, which promotes the property that such values are close to each other. Unfortunately, due to the manifold constrained, this is still a difficult nonconvex problem. Recalling the convexity relaxed model of Condat [16] for circle-valued data, we show how this relaxed model can be nicely simplified without losing any information. Based on Schur complement arguments, we will see that our model leads to the same minimizers while reducing the number of parameters and consequently making the computation more efficient. In a preprint [17], which came without any numerical results, Condat suggested to generalize his model to data on the 2-sphere. In this paper, we will see that this approach can be simplified as well. Moreover, it just appears as a special case of quaternion-valued data processing. The latter one also leads to a relaxed convex model for $SO(3)$ -valued data. In the proceeding [7], we introduce a similar approach for anisotropic TV. Since the TV functional has another structure than the quadratic Tikhonov regularizer, we end up with a completely different convexification.

Outline of the paper: in Section 2, we reconsider Condat’s relaxation of the nonconvex Tikhonov model for denoising circle-valued data. We address the model from two different points of view depending whether we embed the circle into the complex numbers \mathbb{C} or into the real numbers \mathbb{R}^2 . Both viewpoints make it easier to understand the later extension of the approach to the quaternion setting. Then, we introduce our simplified model and prove that this model has the same solutions as the original relaxed formulation by using Schur complement arguments. In Section 3, we will see that our simplified model can be generalized to higher dimensional spheres in a straightforward way. Next, in Section 4, we explain how the nonconvex Tikhonov model as well as its relaxation and simplification can be generalized to $SO(3)$ -valued data. The approach relies on the parameterization of $SO(3)$ by quaternions. Remarkably, it also includes 2-sphere-valued data. We describe the ADMM for finding a minimizer of our relaxed models in Section 5. Finally, Section 6 provides some proof-of-the-concept denoising examples for circle-, sphere- and $SO(3)$ -valued data. Although we cannot prove the tightness of our relaxation, we observe that the calculated numerical solutions solve the original nonconvex problem, i.e. the denoised signals are again circle-, sphere- or $SO(3)$ -valued. In case of circle-valued data, we compare our simplified approach with the original relaxation in [16], where we observe significant improvements concerning the computational complexity and numerical convergence. Additionally, we compare our approach with the TV denoiser from [10], which is based on geodesic distances, where we observe significant improvements concerning the computation time and restoration error.

2 Denoising of Circle-Valued Data

Let $G = (V, E)$ be a connected, undirected graph, where $V := \{1, \dots, N\}$ denotes the set of vertices, and $E \subset \{(n, m) \in V \times V : n < m\}$ the set of edges. The cardinality of E is henceforth denoted by $M := |E|$. Our aim is to denoise a disturbed circle-valued signal on G . The circle can be either embedded into the complex numbers \mathbb{C} or into the two-dimensional Euclidean space \mathbb{R}^2 . The former approach has been especially considered by Condat [16] and is summarized in Section 2.1. The latter

approach proposed by us is studied in Section 2.3 and can be immediately generalized to tackle sphere-valued and SO(3)-valued data, see Section 3 and 4. To show that the complex- and real-valued model are in fact equivalent, we introduce an in-between model in Section 2.2 interpreting the complex-valued approach itself as real-valued problem.

2.1 \mathbb{C} -Valued Model

Let $\mathbb{S}_{\mathbb{C}} := \{z \in \mathbb{C} : |z| = 1\}$ denote the (complex-valued) unit circle. Our aim is to recover an $\mathbb{S}_{\mathbb{C}}$ -valued signal $x := (x_n)_{n \in V} \in \mathbb{S}_{\mathbb{C}}^N$ on G from noisy measurements $y := (y_n)_{n \in V} \in \mathbb{S}_{\mathbb{C}}^N$. Note that the following considerations work also for $y \in \mathbb{C}^N$. A straightforward approach would be to search for the minimizer of the Tikhonov-like regularized functional

$$\arg \min_{x \in \mathbb{S}_{\mathbb{C}}^N} \sum_{n \in V} \frac{w_n}{2} |x_n - y_n|^2 + \sum_{(n,m) \in E} \frac{\lambda_{(n,m)}}{2} |x_n - x_m|^2, \quad (1)$$

where $w := (w_n)_{n \in V} \in \mathbb{R}_+^N$ and $\lambda := (\lambda_{(n,m)})_{(n,m) \in E} \in \mathbb{R}_+^M$ are positive weights. Unfortunately, due to the constraints $x_n \in \mathbb{S}_{\mathbb{C}}$, this problem is nonconvex. In the first step, to derive a convex relaxation, we exploit $|x_n| = 1$

and hence we derive

$$|x_n - y_n|^2 = |x_n|^2 - 2\Re[x_n \bar{y}_n] + |y_n|^2 = -2\Re[x_n \bar{y}_n] + \text{const}$$

and similarly

$$|x_n - x_m|^2 = |x_m|^2 - 2\Re[\bar{x}_m x_n] + |x_n|^2 = -2\Re[\bar{x}_m x_n] + \text{const},$$

where $\Re[z] = \Re[\alpha + i\beta] = \alpha$ for $z = \alpha + i\beta \in \mathbb{C}$ with $\alpha, \beta \in \mathbb{R}$. We rewrite the original problem (1) as

$$\arg \min_{x \in \mathbb{S}_{\mathbb{C}}^N} - \sum_{n \in V} w_n \Re[x_n \bar{y}_n] - \sum_{(n,m) \in E} \lambda_{(n,m)} \Re[\bar{x}_m x_n]. \quad (2)$$

Introducing $r := (r_{(n,m)})_{(n,m) \in E} \in \mathbb{C}^M$, we rearrange the minimization problem (2) into

$$\arg \min_{x \in \mathbb{S}_{\mathbb{C}}^N, r \in \mathbb{C}^M} \mathcal{J}(x, r) \text{ s.t. } r_{(n,m)} = \bar{x}_m x_n \quad (3)$$

for all $(n, m) \in E$ with

$$\mathcal{J}(x, r) := - \sum_{n \in V} w_n \Re[x_n \bar{y}_n] - \sum_{(n,m) \in E} \lambda_{(n,m)} \Re[r_{(n,m)}].$$

The core idea of Condat's convex relaxation [16] is to encode the nonconvex constraint $x \in \mathbb{S}_{\mathbb{C}}^N$ into a positive semi-definite, rank-one matrix.

Lemma 1. *Let $n, m \in V$ and $(n, m) \in E$. Then $x_n, x_m \in \mathbb{S}_{\mathbb{C}}$ and $r_{(n,m)} = \bar{x}_m x_n$ if and only if*

$$P_{(n,m)} := \begin{bmatrix} 1 & x_n & x_m \\ \bar{x}_n & 1 & \bar{r}_{(n,m)} \\ \bar{x}_m & r_{(n,m)} & 1 \end{bmatrix} \in \mathbb{C}^{3 \times 3} \quad (4)$$

is positive semi-definite and has rank one.

Proof. Let $x_n, x_m \in \mathbb{S}_{\mathbb{C}}$ and $r_{(n,m)} = \bar{x}_m x_n$, and denote the conjugation and transposition by $^{\text{H}}$. Then $P_{(n,m)} = (1, x_n, x_m)^{\text{H}} (1, x_n, x_m)$ has rank one and is positive semi-definite. Conversely, positive semi-definiteness and the rank-one condition imply that $P_{(n,m)}$ has the form

$$P_{(n,m)} = (a, b, c)^{\text{H}} (a, b, c) = \begin{bmatrix} \bar{a}a & \bar{a}b & \bar{a}c \\ \bar{b}a & \bar{b}b & \bar{b}c \\ \bar{c}a & \bar{c}b & \bar{c}c \end{bmatrix}$$

for some $a, b, c \in \mathbb{C}$. Comparison with (4) yields $|a| = |b| = |c| = 1$ and thus $|x_n| = |\bar{a}||b| = 1$, $|x_m| = |\bar{a}||c| = 1$ as well as $r_{(n,m)} = \bar{c}b = \bar{c}a\bar{a}b = \bar{x}_m x_n$. \square

We denote the rank function by rk . Based on Lemma 1, Problem (3) and thus the original formulation (1) become

$$\arg \min_{x \in \mathbb{C}^N, r \in \mathbb{C}^M} \mathcal{J}(x, r) \text{ s.t. } P_{(n,m)} \succeq 0 \text{ and } \text{rk}(P_{(n,m)}) = 1$$

for all $(n, m) \in E$. Neglecting the rank-one constraint, Condat [16] proposes to solve the relaxation:

relaxed complex model

$$\arg \min_{x \in \mathbb{C}^N, r \in \mathbb{C}^M} \mathcal{J}(x, r) \text{ s.t. } P_{(n,m)} \succeq 0 \quad (5)$$

for all $(n, m) \in E$. Since (5) is a convex optimization problem, we may apply standard methods from convex analysis to obtain numerical solutions.

2.2 Related \mathbb{R}^2 -Valued Model

Alternatively, the sphere can be embedded in the Euclidean space \mathbb{R}^2 equipped with the Euclidean norm $\|\cdot\|$ and inner product $\langle \cdot, \cdot \rangle$. To emphasize the relation to the complex-valued model, we identify the complex number $z \in \mathbb{C}$ with the two-dimensional Euclidean vector $\mathbf{z} := (\Re[z], \Im[z])^T \in \mathbb{R}^2$, where \cdot^T denotes the transposition. Against this background, we denote the first and second component of \mathbf{z} by $\Re[\mathbf{z}] := \mathbf{z}_1$ and $\Im[\mathbf{z}] := \mathbf{z}_2$ respectively. Defining $\mathbb{S}_1 := \{\mathbf{z} \in \mathbb{R}^2 : \|\mathbf{z}\| = 1\}$, we now want to recover an \mathbb{S}_1 -valued signal $\mathbf{x} := (\mathbf{x}_n)_{n \in V} \in \mathbb{S}_1^N$ on G from noisy measurements $\mathbf{y} := (\mathbf{y}_n)_{n \in V} \in (\mathbb{S}_1)^N$. Exploiting $|z| = \|\mathbf{z}\|$ for all $z \in \mathbb{C}$, we rewrite (1) into the real-valued model

$$\arg \min_{\mathbf{x} \in \mathbb{S}_1^N} \sum_{n \in V} \frac{w_n}{2} \|\mathbf{x}_n - \mathbf{y}_n\|^2 + \sum_{(n,m) \in E} \frac{\lambda_{(n,m)}}{2} \|\mathbf{x}_n - \mathbf{x}_m\|^2. \quad (6)$$

To transfer the relaxation of the complex model, we exploit that the complex multiplication can be realized using the matrix representation of $z \in \mathbb{C}$ given by

$$\mathbf{M}(z) := \mathbf{M}(\mathbf{z}) := \begin{bmatrix} \Re[\mathbf{z}] & -\Im[\mathbf{z}] \\ \Im[\mathbf{z}] & \Re[\mathbf{z}] \end{bmatrix}.$$

Introducing the variables $\mathbf{r}_{(n,m)} = \mathbf{M}(\mathbf{x}_m)^T \mathbf{x}_n \in \mathbb{R}^2$, the real-valued version of (3) reads as

$$\arg \min_{\mathbf{x} \in \mathbb{S}_1^N, \mathbf{r} \in (\mathbb{R}^2)^M} \mathcal{J}(\mathbf{x}, \mathbf{r}) \text{ s.t. } \mathbf{r}_{(n,m)} = \mathbf{M}(\mathbf{x}_m)^T \mathbf{x}_n \quad (7)$$

for all $(n, m) \in E$ with

$$\mathcal{J}(\mathbf{x}, \mathbf{r}) := - \sum_{n \in V} w_n \langle \mathbf{x}_n, \mathbf{y}_n \rangle - \sum_{(n,m) \in E} \lambda_{(n,m)} \Re[\mathbf{r}_{(n,m)}]. \quad (8)$$

Note that \mathcal{J} does not depend on $\Im[\mathbf{r}_{(n,m)}]$ and is an artifact of the complex viewpoint. In Section 2.3, we show that this auxiliary variable can indeed be dropped from the optimization without changing the minimizer. Denoting the $d \times d$ identity matrix by \mathbf{I}_d , where the index is omitted if the dimension is clear, we analogously encode the nonconvex constraint of (7) into a matrix expression.

Lemma 2. *Let $n, m \in V$ and $(n, m) \in E$. Then $\mathbf{x}_n, \mathbf{x}_m \in \mathbb{S}_1$ and $\mathbf{r}_{(n,m)} = \mathbf{M}(\mathbf{x}_m)^T \mathbf{x}_n$ if and only if the block matrix*

$$\mathbf{P}_{(n,m)} := \begin{bmatrix} \mathbf{I}_2 & \mathbf{M}(\mathbf{x}_n) & \mathbf{M}(\mathbf{x}_m) \\ \mathbf{M}(\mathbf{x}_n)^T & \mathbf{I}_2 & \mathbf{M}(\mathbf{r}_{(n,m)})^T \\ \mathbf{M}(\mathbf{x}_m)^T & \mathbf{M}(\mathbf{r}_{(n,m)}) & \mathbf{I}_2 \end{bmatrix} \in \mathbb{R}^{6 \times 6}$$

is positive semi-definite and has rank two.

Proof. Let the conditions for $\mathbf{x}_n, \mathbf{x}_m$ and $\mathbf{r}_{(n,m)}$ be fulfilled. Since $\mathbf{M}(\mathbf{x}_n)^T \mathbf{M}(\mathbf{x}_n) = \|\mathbf{x}_n\|^2 \mathbf{I}_2$ and $\mathbf{M}(\mathbf{x}_m)^T \mathbf{M}(\mathbf{x}_m) = \mathbf{M}(\mathbf{r}_{(n,m)})$, we obtain

$$\mathbf{P}_{(n,m)} = [\mathbf{I}_2, \mathbf{M}(\mathbf{x}_n), \mathbf{M}(\mathbf{x}_m)]^T [\mathbf{I}_2, \mathbf{M}(\mathbf{x}_n), \mathbf{M}(\mathbf{x}_m)]$$

implying $\text{rk}(\mathbf{P}_{(n,m)}) = 2$ and $\mathbf{P}_{(n,m)} \succeq 0$. The opposite direction follows similarly as in the proof of Lemma 1. \square

Due to Lemma 2, the real-valued formulation (7) becomes

$$\arg \min_{\substack{\mathbf{x} \in (\mathbb{R}^2)^N \\ \mathbf{r} \in (\mathbb{R}^2)^M}} \mathcal{J}(\mathbf{x}, \mathbf{r}) \text{ s.t. } \mathbf{P}_{(n,m)} \succeq 0 \text{ and } \text{rk}(\mathbf{P}_{(n,m)}) = 2 \quad (9)$$

for all $(n, m) \in E$. Since obviously $\mathbf{P}_{(n,m)} \succeq 0$ if and only if $P_{(n,m)} \succeq 0$ from (4), neglecting the rank-two constraint in (9) yields the relaxed formulation:

$$\begin{aligned} & \text{relaxed real model} \\ & \arg \min_{\mathbf{x} \in (\mathbb{R}^2)^N, \mathbf{r} \in (\mathbb{R}^2)^M} \mathcal{J}(\mathbf{x}, \mathbf{r}) \text{ s.t. } \mathbf{P}_{(n,m)} \succeq 0 \end{aligned} \quad (10)$$

for all $(n, m) \in E$, which is just the real-valued version of complex relaxation (5).

2.3 Simplified \mathbb{R}^2 -Valued Model

Note that the seconds variables $\mathbf{r}_{(n,m)} = \mathbf{M}(\mathbf{x}_m)^\top \mathbf{x}_n$ in (7) are artificial and originate from the complex-valued model. Therefore the minimization problem (7) seems to be needlessly puffed-up since we also optimize with respect to the variables $\mathfrak{S}(\mathbf{r}_{(n,m)})$ that do not influence the objective \mathcal{J} in (8) at all. To this end, we propose to reformulate the real-valued problem (6) as

$$\arg \min_{\mathbf{x} \in \mathbb{S}_1^N, \boldsymbol{\ell} \in \mathbb{R}^M} \mathcal{K}(\mathbf{x}, \boldsymbol{\ell}) \text{ s.t. } \boldsymbol{\ell}_{(n,m)} = \langle \mathbf{x}_n, \mathbf{x}_m \rangle$$

for all $(n, m) \in E$ with

$$\mathcal{K}(\mathbf{x}, \boldsymbol{\ell}) := - \sum_{n \in V} w_n \langle \mathbf{x}_n, \mathbf{y}_n \rangle - \sum_{(n,m) \in E} \lambda_{(n,m)} \boldsymbol{\ell}_{(n,m)},$$

using a similar rewriting process for the squared 2-norm as in the previous sections. As before and with a similar proof, the nonconvex constraints $\mathbf{x}_n \in \mathbb{S}_1$ and $\boldsymbol{\ell}_{(n,m)} = \langle \mathbf{x}_n, \mathbf{x}_m \rangle$ may be encoded using the positive semi-definiteness and a rank condition of an appropriate matrix.

Lemma 3. *Let $n, m \in V$ and $(n, m) \in E$. Then $\mathbf{x}_n, \mathbf{x}_m \in \mathbb{S}_1$ and $\boldsymbol{\ell}_{(n,m)} = \langle \mathbf{x}_n, \mathbf{x}_m \rangle$ if and only if the block matrix*

$$\mathbf{Q}_{(n,m)} := \begin{bmatrix} \mathbf{I}_2 & \mathbf{x}_n & \mathbf{x}_m \\ \mathbf{x}_n^\top & 1 & \boldsymbol{\ell}_{(n,m)} \\ \mathbf{x}_m^\top & \boldsymbol{\ell}_{(n,m)} & 1 \end{bmatrix} \in \mathbb{R}^{4 \times 4}$$

is positive semi-definite and has rank two.

In this paper, we relax the rank-two constraint and propose to solve our new relaxed formulation:

$$\begin{aligned} & \text{simplified relaxed real model} \\ & \arg \min_{\mathbf{x} \in (\mathbb{R}^2)^N, \boldsymbol{\ell} \in \mathbb{R}^M} \mathcal{K}(\mathbf{x}, \boldsymbol{\ell}) \text{ s.t. } \mathbf{Q}_{(n,m)} \succeq 0 \end{aligned} \quad (11)$$

for all $(n, m) \in E$. Our convex model (11) is simpler than (10), since $\mathbf{r}_{(n,m)} \in \mathbb{R}^2$ is replaced by $\boldsymbol{\ell}_{(n,m)} \in \mathbb{R}$. Nevertheless, both problems lead to the same solutions. To show this, we need a result on the Schur complement of matrices.

Proposition 4 ([24, p. 495]). *For invertible $\mathbf{A} \in \mathbb{R}^{\ell \times \ell}$, it holds*

$$\mathbf{W} = \begin{bmatrix} \mathbf{A} & \mathbf{C} \\ \mathbf{C}^\top & \mathbf{B} \end{bmatrix} = \begin{bmatrix} \mathbf{I} & \mathbf{0} \\ \mathbf{C}^\top \mathbf{A}^{-1} & \mathbf{I} \end{bmatrix} \begin{bmatrix} \mathbf{A} & \mathbf{0} \\ \mathbf{0} & \mathbf{B} - \mathbf{C}^\top \mathbf{A}^{-1} \mathbf{C} \end{bmatrix} \begin{bmatrix} \mathbf{I} & \mathbf{A}^{-1} \mathbf{C} \\ \mathbf{0}^\top & \mathbf{I} \end{bmatrix} \in \mathbb{R}^{\ell+n \times \ell+n},$$

where $\mathbf{B} \in \mathbb{R}^{n \times n}$ and $\mathbf{C} \in \mathbb{R}^{\ell \times n}$. The matrix $\mathbf{W}/\mathbf{A} := \mathbf{B} - \mathbf{C}^\top \mathbf{A}^{-1} \mathbf{C} \in \mathbb{R}^{n \times n}$ is called Schur complement of \mathbf{W} and we have $\mathbf{W} \succeq 0$ if and only if $\mathbf{A} \succ 0$ and $\mathbf{W}/\mathbf{A} \succeq 0$.

Now we can prove the main equivalence theorem.

Theorem 5. Problems (10) and (11) are equivalent in the following sense:

- (i) If $(\hat{\mathbf{x}}, \hat{\mathbf{r}})$ solves (10), then $(\hat{\mathbf{x}}, \Re[\hat{\mathbf{r}}])$ solves (11).
- (ii) If $(\tilde{\mathbf{x}}, \tilde{\ell})$ solves (11), then $(\tilde{\mathbf{x}}, \tilde{\mathbf{r}})$ with $\tilde{\mathbf{r}}_{(n,m)} = (\tilde{\ell}_{(n,m)}, \Im[\mathbf{M}(\tilde{\mathbf{x}}_m)^\top \tilde{\mathbf{x}}_n])^\top$ solves (10).

Proof. The Schur complement of $\mathbf{Q}_{m,n}$ with respect to \mathbf{I}_2 is given by

$$\mathbf{Q}_{(n,m)}/\mathbf{I}_2 = \begin{bmatrix} 1 - |\mathbf{x}_n|^2 & \ell_{(n,m)} - \langle \mathbf{x}_n, \mathbf{x}_m \rangle \\ \ell_{(n,m)} - \langle \mathbf{x}_n, \mathbf{x}_m \rangle & 1 - |\mathbf{x}_m|^2 \end{bmatrix} \quad (12)$$

On the other hand, permuting the fourth and fifth column/row of $\mathbf{P}_{(n,m)}$, we obtain

$$\tilde{\mathbf{P}}_{(n,m)} := \left[\begin{array}{cc|cc|cc} 1 & 0 & \Re[\mathbf{x}_n] & \Re[\mathbf{x}_m] & -\Im[\mathbf{x}_n] & -\Im[\mathbf{x}_m] \\ 0 & 1 & \Im[\mathbf{x}_n] & \Im[\mathbf{x}_m] & \Re[\mathbf{x}_n] & \Re[\mathbf{x}_m] \\ \hline \Re[\mathbf{x}_n] & \Im[\mathbf{x}_n] & 1 & \Re[\mathbf{r}_{(n,m)}] & 0 & \Im[\mathbf{r}_{(n,m)}] \\ \Re[\mathbf{x}_m] & \Im[\mathbf{x}_m] & \Re[\mathbf{r}_{(n,m)}] & 1 & -\Im[\mathbf{r}_{(n,m)}] & 0 \\ \hline -\Im[\mathbf{x}_n] & \Re[\mathbf{x}_n] & 0 & -\Im[\mathbf{r}_{(n,m)}] & 1 & \Re[\mathbf{r}_{(n,m)}] \\ -\Im[\mathbf{x}_m] & \Re[\mathbf{x}_m] & \Im[\mathbf{r}_{(n,m)}] & 0 & \Re[\mathbf{r}_{(n,m)}] & 1 \end{array} \right],$$

which has the Schur complement

$$\tilde{\mathbf{P}}_{(n,m)}/\mathbf{I}_2 = \left[\begin{array}{cc|cc} 1 - |\mathbf{x}_n|^2 & \Re[\mathbf{r}_{(n,m)}] - \Re[\mathbf{M}(\mathbf{x}_m)^\top \mathbf{x}_n] & 0 & \Im[\mathbf{r}_{(n,m)}] - \Im[\mathbf{M}(\mathbf{x}_m)^\top \mathbf{x}_n] \\ \Re[\mathbf{r}_{(n,m)}] - \Re[\mathbf{M}(\mathbf{x}_m)^\top \mathbf{x}_n] & 1 - |\mathbf{x}_m|^2 & -\Im[\mathbf{r}_{(n,m)}] + \Im[\mathbf{M}(\mathbf{x}_m)^\top \mathbf{x}_n] & 0 \\ \hline 0 & -\Im[\mathbf{r}_{(n,m)}] + \Im[\mathbf{M}(\mathbf{x}_m)^\top \mathbf{x}_n] & 1 - |\mathbf{x}_n|^2 & \Re[\mathbf{r}_{(n,m)}] - \Re[\mathbf{M}(\mathbf{x}_m)^\top \mathbf{x}_n] \\ \Im[\mathbf{r}_{(n,m)}] - \Im[\mathbf{M}(\mathbf{x}_m)^\top \mathbf{x}_n] & 0 & \Re[\mathbf{r}_{(n,m)}] - \Re[\mathbf{M}(\mathbf{x}_m)^\top \mathbf{x}_n] & 1 - |\mathbf{x}_m|^2 \end{array} \right]. \quad (13)$$

Recall that $\Re[\mathbf{M}(\mathbf{x}_m)^\top \mathbf{x}_n] = \langle \mathbf{x}_n, \mathbf{x}_m \rangle$. Using the Schur complements in (12) and (13) as well as Proposition 4, we obtain the following: if $(\hat{\mathbf{x}}, \hat{\mathbf{r}})$ solves (10), then $(\hat{\mathbf{x}}, \hat{\ell})$ with $\hat{\ell} := \Re[\hat{\mathbf{r}}]$ is a feasible point of (11). Moreover, it holds by their definition that $\mathcal{K}(\hat{\mathbf{x}}, \hat{\ell}) = \mathcal{J}(\hat{\mathbf{x}}, \hat{\mathbf{r}})$.

Conversely, if $(\tilde{\mathbf{x}}, \tilde{\ell})$ solves (11), then $(\tilde{\mathbf{x}}, \tilde{\mathbf{r}})$ with $\tilde{\mathbf{r}}$ defined in the theorem is a feasible point of (10). Further, we have $\mathcal{K}(\tilde{\mathbf{x}}, \tilde{\ell}) = \mathcal{J}(\tilde{\mathbf{x}}, \tilde{\mathbf{r}})$. Taking the minimizing property into account, we conclude

$$\mathcal{K}(\tilde{\mathbf{x}}, \tilde{\ell}) \leq \mathcal{K}(\hat{\mathbf{x}}, \hat{\ell}) = \mathcal{J}(\hat{\mathbf{x}}, \hat{\mathbf{r}}) \leq \mathcal{J}(\tilde{\mathbf{x}}, \tilde{\mathbf{r}}) = \mathcal{K}(\tilde{\mathbf{x}}, \tilde{\ell}),$$

which is only possible if all values coincide. \square

Our previous considerations yield immediately the following corollary.

Corollary 6. Problems (5) and (11) are equivalent in the following sense:

- (i) If $(\hat{\mathbf{x}}, \hat{\mathbf{r}})$ solves (5), then $(\hat{\mathbf{x}}, \Re[\hat{\mathbf{r}}])$ solves (11).
- (ii) If $(\tilde{\mathbf{x}}, \tilde{\ell})$ solves (11), then $(\tilde{\mathbf{x}}, \tilde{\mathbf{r}})$ with $\tilde{\mathbf{r}}_{(n,m)} = \tilde{\ell}_{(n,m)} + i\Im[\tilde{\mathbf{x}}_m \tilde{\mathbf{x}}_n]$ solves (10).

3 Generalization to Sphere-Valued Data

The main advantage of the real-valued, relaxed model (11) is its simple generalization to higher dimensions,

which we derive in this section. Defining the $(d-1)$ -dimensional sphere as $\mathbb{S}_{d-1} := \{\mathbf{x} \in \mathbb{R}^d : \|\mathbf{x}\| = 1\}$, we aim to determine the signal $\mathbf{x} := (\mathbf{x}_n)_{n \in V} \in \mathbb{S}_{d-1}^N$ on G from perturbed values $\mathbf{y} := (\mathbf{y}_n)_{n \in V} \in (\mathbb{S}_{d-1})^N$. Note that the following relaxation remains valid for $\mathbf{y}_n \in \mathbb{R}^d$. We start with the original, nonconvex problem

$$\arg \min_{\mathbf{x} \in \mathbb{S}_{d-1}^N} \sum_{n \in V} \frac{w_n}{2} \|\mathbf{x}_n - \mathbf{y}_n\|^2 + \sum_{(n,m) \in E} \frac{\lambda_{(n,m)}}{2} \|\mathbf{x}_n - \mathbf{x}_m\|^2, \quad (14)$$

and its rewritten version

$$\arg \min_{\mathbf{x} \in \mathbb{S}_{d-1}^N, \ell \in \mathbb{R}^M} \mathcal{K}(\mathbf{x}, \ell) \quad \text{s.t.} \quad \ell_{(n,m)} = \langle \mathbf{x}_n, \mathbf{x}_m \rangle$$

for all $(n,m) \in E$ with

$$\mathcal{K}(\mathbf{x}, \ell) := - \sum_{n \in V} w_n \langle \mathbf{x}_n, \mathbf{y}_n \rangle - \sum_{(n,m) \in E} \lambda_{(n,m)} \ell_{(n,m)}$$

similar to the embedding in the 2-dimensional Euclidean vector space. Immediately, Lemma 3 extends to higher dimensions as follows.

Lemma 7. Let $n, m \in V$ and $(n, m) \in E$. Then $\mathbf{x}_n, \mathbf{x}_m \in \mathbb{S}_{d-1}$ and $\boldsymbol{\ell}_{(n,m)} = \langle \mathbf{x}_n, \mathbf{x}_m \rangle$ if and only if the block matrix

$$\mathbf{Q}_{(n,m)} := \begin{bmatrix} \mathbf{I}_d & \mathbf{x}_n & \mathbf{x}_m \\ \mathbf{x}_n^\top & 1 & \boldsymbol{\ell}_{(n,m)} \\ \mathbf{x}_m^\top & \boldsymbol{\ell}_{(n,m)} & 1 \end{bmatrix} \in \mathbb{R}^{(d+2) \times (d+2)}$$

is positive semi-definite and has rank d .

Incorporating Lemma 7 and relaxing the rank- d constraint, we obtain the new d -dimensional generalization:

simplified relaxed real model

$$\arg \min_{\mathbf{x} \in (\mathbb{R}^d)^N, \boldsymbol{\ell} \in \mathbb{R}^M} \mathcal{K}(\mathbf{x}, \boldsymbol{\ell}) \quad \text{s.t.} \quad \mathbf{Q}_{(n,m)} \succeq 0 \quad (15)$$

for all $(n, m) \in E$, which is again a real-valued, convex optimization problem and can thus be solved applying standard numerical methods from convex analysis. From a theoretical point of view, the tightness of the simplified relaxed real model to the original nonconvex problem remains an open issue, i.e., having a solution of (15), it is unclear how to construct a solution of (14). From a numerical point of view, we observe in our experiments that the calculated solutions of (15) immediately solve (14).

4 Generalization to SO(3)-Valued Data

In some applications like electron backscatter tomography, the measured data naturally lie on the 3d rotation group $\text{SO}(3) := \{\mathbf{R} \in \mathbb{R}^{3,3} : \mathbf{R}^\top \mathbf{R} = \mathbf{I}_3, \det(\mathbf{R}) = 1\}$. The matrices in $\text{SO}(3)$ form a three-dimensional manifold and can be parameterized using the rotation axis $\mathbf{v} \in \mathbb{S}_2$ and the rotation angle $\alpha \in [-\pi, \pi)$. More precisely, the rotation matrix corresponding to \mathbf{v} and α is given by

$$\mathbf{R}(\mathbf{v}, \alpha) := \begin{bmatrix} (1-\cos(\alpha)) \mathbf{v}_1^2 + \cos(\alpha) & (1-\cos(\alpha)) \mathbf{v}_1 \mathbf{v}_2 - \mathbf{v}_3 \sin(\alpha) & (1-\cos(\alpha)) \mathbf{v}_1 \mathbf{v}_3 + \mathbf{v}_2 \sin(\alpha) \\ (1-\cos(\alpha)) \mathbf{v}_2 \mathbf{v}_1 + \mathbf{v}_3 \sin(\alpha) & (1-\cos(\alpha)) \mathbf{v}_2^2 + \cos(\alpha) & (1-\cos(\alpha)) \mathbf{v}_2 \mathbf{v}_3 - \mathbf{v}_1 \sin(\alpha) \\ (1-\cos(\alpha)) \mathbf{v}_1 \mathbf{v}_3 - \mathbf{v}_2 \sin(\alpha) & (1-\cos(\alpha)) \mathbf{v}_3 \mathbf{v}_2 + \mathbf{v}_1 \sin(\alpha) & (1-\cos(\alpha)) \mathbf{v}_3^2 + \cos(\alpha) \end{bmatrix}.$$

Due to $\mathbf{R}(\mathbf{v}, \alpha) = \mathbf{R}(-\mathbf{v}, -\alpha)$, the rotation angle may be restricted to $\alpha \in [0, \pi)$. Moreover, $\text{SO}(3)$ can be parameterized by unit quaternions, see for instance [21], which allow us to apply the derived methods to denoise $\text{SO}(3)$ -valued data.

Each quaternion $z \in \mathbb{H}$ can be written as $z := z_1 + iz_2 + jz_3 + kz_4$ with $z_1, z_2, z_3, z_4 \in \mathbb{R}$, where the symbols i, j, k generalize the complex-imaginary unit. The noncommutative multiplication of two quaternions is defined by the table

$$\begin{aligned} i^2 = j^2 = k^2 &= -1, & ij = -ji = k, \\ jk = -kj = i, & ki = -ik = j. \end{aligned}$$

The *conjugate* of a quaternion is given by $\bar{z} := z_1 - iz_2 - jz_3 - kz_4$, and its *norm* by $|z|^2 := \bar{z}z = z\bar{z}$. The *real* or *scalar part* of z is denoted by $\Re[z] := z_1$, and its *imaginary* or *vector part* by $\Im[z] := iz_2 + jz_3 + kz_4$. Note that, different from the complex-imaginary part, the quaternion-imaginary part contains the symbols i, j, k . The real components to the symbols are henceforth denoted by $\Im_i[z] := z_2, \Im_j[z] := z_3, \Im_k[z] := z_4$. The sphere of the unit quaternions is indicated by $\mathbb{S}_{\mathbb{H}} := \{z \in \mathbb{H} : |z| = 1\}$.

The action of rotations in $\text{SO}(3)$ can now be identified with the action of unit quaternions [21]. For this, we identify the rotation axis $\mathbf{v} \in \mathbb{S}_2$ and angle $\alpha \in [-\pi, \pi)$ with the unit quaternion

$$q(\mathbf{v}, \alpha) := \cos\left(\frac{\alpha}{2}\right) + \sin\left(\frac{\alpha}{2}\right) (i\mathbf{v}_1 + j\mathbf{v}_2 + k\mathbf{v}_3). \quad (16)$$

Notice that the real part of $q(\mathbf{v}, \alpha)$ is always nonnegative. The rotation of $\mathbf{x} \in \mathbb{R}^3$ is given by

$$\mathbf{R}(\mathbf{v}, \alpha) \mathbf{x} = (\Im_i[\xi_{\mathbf{x}}], \Im_j[\xi_{\mathbf{x}}], \Im_k[\xi_{\mathbf{x}}])^\top$$

with the quaternion

$$\xi_{\mathbf{x}} := q(\mathbf{v}, \alpha) (i\mathbf{x}_1 + j\mathbf{x}_2 + k\mathbf{x}_3) \bar{q}(\mathbf{v}, \alpha),$$

i.e. the action of the rotation corresponds to a conjugation in the group of the unit quaternions. Obviously, the unit quaternions q and $-q$ correspond to the same rotation. More precisely, the unit quaternions form a double cover of $\text{SO}(3)$ by

$$\mathbb{S}_{\mathbb{H}}/\{-1, 1\} \cong \text{SO}(3),$$

where $q_1, q_2 \in \mathbb{S}_{\mathbb{H}}$ are equivalent if $q_1 \bar{q}_2 \in \{-1, 1\}$, see [12, Ch III, § 10]. The other way round, the unit quaternion $q \in \mathbb{S}_{\mathbb{H}}/\{-1, 1\}$ corresponds to the rotation matrix

$$\mathbf{R}(q) := \begin{bmatrix} 1-2\Im_j[q]^2-2\Im_k[q]^2 & 2\Im_i[q]\Im_j[q]-2\Im_k[q]\Re[q] & 2\Im_i[q]\Im_k[q]+2\Im_j[q]\Re[q] \\ 2\Im_i[q]\Im_j[q]+2\Im_k[q]\Re[q] & 1-2\Im_i[q]^2-2\Im_k[q]^2 & 2\Im_j[q]\Im_k[q]-2\Im_i[q]\Re[q] \\ 2\Im_i[q]\Im_k[q]-2\Im_j[q]\Re[q] & 2\Im_j[q]\Im_k[q]+2\Im_i[q]\Re[q] & 1-2\Im_i[q]^2-2\Im_j[q]^2 \end{bmatrix}.$$

Due to the parametrization of $\text{SO}(3)$ by the unit quaternions, we are especially interested in the generalization of the complex-valued model (1) and its convex relaxation (5) to the hypercomplex numbers \mathbb{H} . The aim is again to recover the signal $x := (x_n)_{n \in V} \in \mathbb{S}_{\mathbb{H}}^N$ on G from noisy measurements $y := (y_n)_{n \in V} \in \mathbb{S}_{\mathbb{H}}^N$. Similarly to the complex-valued setting, we consider the nonconvex problem

$$\arg \min_{x \in \mathbb{S}_{\mathbb{H}}^N} \sum_{n \in V} \frac{w_n}{2} |x_n - y_n|^2 + \sum_{(n,m) \in E} \frac{\lambda_{(n,m)}}{2} |x_n - x_m|^2,$$

which is equivalent to

$$\arg \min_{x \in \mathbb{S}_{\mathbb{H}}^N, r \in \mathbb{H}^M} \mathcal{J}(x, r) \quad \text{s.t.} \quad r_{(n,m)} = \bar{x}_m x_n \quad (17)$$

for all $(n, m) \in E$ with

$$\mathcal{J}(x, r) := - \sum_{n \in V} w_n \Re[x_n \bar{y}_n] - \sum_{(n,m) \in E} \lambda_{(n,m)} \Re[r_{(n,m)}].$$

Since the quaternions are noncommutative, the order of multiplication in the constraint $r_{(n,m)} = \bar{x}_m x_n$ matters.

Many concepts of linear algebra generalize to quaternion matrices [43]. A quaternion matrix $A \in \mathbb{H}^{d \times d}$ is called *Hermitian* if $A = A^{\text{H}}$. Such a matrix A is positive semi-definite if $z^{\text{H}} A z \geq 0$ for all $z \in \mathbb{H}^d$. Further, A has rank one if all columns are *right* linear dependent and all rows are *left* linear dependent. Here the term *left* and *right* indicate from which side the quaternion coefficients are multiplied. In the Hermitian case, A has rank one if there exists $z \in \mathbb{H}^d$ such that $A = z z^{\text{H}}$. Using a similar argumentation as in Lemma 1, we can rewrite the nonconvex constraints in terms of quaternion matrices.

Lemma 8. *Let $n, m \in V$ and $(n, m) \in E$. Then $x_n, x_m \in \mathbb{S}_{\mathbb{H}}$ and $r_{(n,m)} = \bar{x}_m x_n$ if and only if*

$$P_{(n,m)} := \begin{bmatrix} 1 & x_n & x_m \\ \bar{x}_n & 1 & \bar{r}_{(n,m)} \\ \bar{x}_m & r_{(n,m)} & 1 \end{bmatrix} \in \mathbb{H}^{3 \times 3} \quad (18)$$

is positive semi-definite and has rank one.

Incorporating Lemma 8 into (17), and relaxing the rank-one constraint, we obtain the new quaternion relaxation:

relaxed quaternion model

$$\arg \min_{x \in \mathbb{H}^N, r \in \mathbb{H}^M} \mathcal{J}(x, r) \quad \text{s.t.} \quad P_{(n,m)} \succeq 0 \quad (19)$$

for all $(n, m) \in E$. This is the generalization of Condat's relaxed complex model (5) for quaternion-valued data. Using the approach as for complex data, we identify the quaternion $x_n \in \mathbb{H}$ with the vector

$\mathbf{x}_n := (\Re[x_n], \Im_i[x_n], \Im_j[x_n], \Im_k[x_n])^T \in \mathbb{R}^4$ and propose to solve instead of (19) again our new simplified relaxed real model (15) with $d = 4$, i.e. we propose to solve the convex formulation:

simplified relaxed real model

$$\arg \min_{\mathbf{x} \in (\mathbb{R}^4)^N, \boldsymbol{\ell} \in \mathbb{R}^M} \mathcal{K}(\mathbf{x}, \boldsymbol{\ell}) \quad \text{s.t.} \quad \mathbf{Q}_{(n,m)} \succeq 0 \quad (20)$$

for all $(n, m) \in E$, where

$$\mathbf{Q}_{(n,m)} := \begin{bmatrix} \mathbf{I}_4 & \mathbf{x}_n & \mathbf{x}_m \\ \mathbf{x}_n^T & 1 & \boldsymbol{\ell}_{(n,m)} \\ \mathbf{x}_m^T & \boldsymbol{\ell}_{(n,m)} & 1 \end{bmatrix} \in \mathbb{R}^{6 \times 6}. \quad (21)$$

Note that this is exactly the simplified relaxed real model for \mathbb{S}_3 -valued data. Similarly to Corollary 6, the following theorem establishes that the relaxed quaternion model (19) is equivalent to the simplified relaxed real one (20).

Theorem 9. *Problems (19) and (20) are equivalent in the following sense:*

- (i) *If (\hat{x}, \hat{r}) solves (19), then $(\hat{\mathbf{x}}, \Re[\hat{r}])$ solves (20).*
- (ii) *If $(\tilde{\mathbf{x}}, \tilde{\boldsymbol{\ell}})$ solves (20), then (\tilde{x}, \tilde{r}) with $\tilde{r}_{(n,m)} = \tilde{\boldsymbol{\ell}}_{(n,m)} + \Im[\tilde{x}_m \tilde{x}_n]$ solves (19).*

Proof. See Appendix. □

Returning to 3d rotations, we want to employ the simplified relaxed real model (20) to denoise $\text{SO}(3)$ -valued signals. More precisely, having given perturbed data $(\mathbf{Y}_n)_{n \in V} \in (\text{SO}(3))^N$, we are looking for a smoothed signal $(\mathbf{X}_n)_{n \in V} \in (\text{SO}(3))^N$. As discussed above, the central idea is to use the double cover $\text{SO}(3) \cong \mathbb{S}_{\mathbb{H}} / \{-1, 1\}$ to lift the given data $(\mathbf{Y}_n)_{n \in V}$ to a quaternion signal $(y_n)_{n \in V} \in \mathbb{S}_{\mathbb{H}}^N$. The main issue is here which sign of the corresponding quaternion should we choose? Assuming that $(\mathbf{Y}_n)_{n \in V}$ originates from a “smooth” signal on G , we expect the Frobenius norm

$$\|\mathbf{Y}_n - \mathbf{Y}_m\|_F^2 = 8(1 - \Re[y_n \bar{y}_m])^2$$

to be relatively small for all $(n, m) \in E$. The identity can be found in [25, Eq. (27)] for instance. Transferring the smoothness assumption, we thus assume that $\Re[y_n \bar{y}_m] \gg 0$ for all $(n, m) \in E$. Starting from an arbitrary lifting of \mathbf{Y}_1 , we lift the remaining data \mathbf{Y}_n such that $\Re[y_n \bar{y}_m] \geq 0$ for $(n, m) \in E$. This lifting process is always successful for any signal on a line-graph or tree. During our numerical simulations, we do not face any inconsistencies in finding a global lifting on well-connected graphs like the image graph. Using the simplified real model (20) and Theorem 9, we determine a smoothed signal $(x_n)_{n \in V} \in \mathbb{S}_{\mathbb{H}}^N$, which is retracted by $\mathbf{X}_n := \mathbf{R}(x_n)$.

Remark 10 (\mathbb{S}_2 -Valued Data). Note that purely imaginary quaternions, i.e. $z \in \mathbb{H}$ with $\Re[z] = 0$, can be identified with three-dimensional vectors. Therefore, the restriction of $\mathbb{S}_{\mathbb{H}}$ to the purely imaginary quaternions can be identified with \mathbb{S}_2 . A variation of Lemma 8 shows that $x_n, x_m \in \mathbb{S}_{\mathbb{H}}$ with $\Re[x_n] = \Re[x_m] = 0$ and $r_{(n,m)} = \bar{x}_m x_n$ if and only if

$$P'_{(n,m)} := \begin{bmatrix} 1 & \Im[x_n] & \Im[x_m] \\ -\Im[x_n] & 1 & \tilde{r}_{(n,m)} \\ -\Im[x_m] & \tilde{r}_{(n,m)} & 1 \end{bmatrix} \in \mathbb{H}^{3 \times 3}$$

is positive semi-definite with rank one. The corresponding *relaxed purely quaternion model*

$$\arg \min_{\mathbf{x} \in \mathbb{H}^N, \mathbf{r} \in \mathbb{H}^M} \mathcal{J}(\mathbf{x}, \mathbf{r}) \quad \text{s.t.} \quad P'_{(n,m)} \succeq 0 \quad \text{for all } (n, m) \in E$$

becomes completely independent of the real parts $\Re[x_n]$, $n \in V$. Setting these real parts to zero, we can use the relaxed quaternion problem for denoising \mathbb{S}_2 -valued data. Furthermore, in line with Theorem 9, the relaxed purely quaternion problem coincides with model (15) for $d = 3$. A similar approach has also been proposed by Condat in [17].

Remark 11 (Octonion-Valued Data). Replacing the quaternions by octonions or more general hypercomplex numbers, we may generalize (19) to more general spheres. Since the octonions are nonassociative, there exists however no real-valued matrix representation, which preserve addition and multiplication. Therefore, Lemma 2 will not carry over to octonions, and the relation between the resulting relaxed octonion model and our simplified relaxed real model with $d = 8$ proposed in Section 3 remains unclear.

5 Algorithm

For numerical simulations, we solve the derived relaxed minimization problems by applying the Alternating Directions Methods of Multipliers (ADMM) [11, 32]. Exemplary, we consider the simplified relaxed d -dimensional real model (15), which can be rewritten as

$$\arg \min_{\substack{\mathbf{x} \in (\mathbb{R}^d)^N, \boldsymbol{\ell} \in \mathbb{R}^M, \\ \mathbf{U} \in (\mathbb{R}^{(d+2) \times (d+2)})^M}} \mathcal{K}(\mathbf{x}, \boldsymbol{\ell}) + \mathcal{G}(\mathbf{U}) \quad \text{s.t.} \quad \mathcal{Q}(\mathbf{x}, \boldsymbol{\ell}) = \mathbf{U}, \quad (22)$$

where the linear map $\mathcal{Q}: (\mathbb{R}^d)^N \times \mathbb{R}^M \rightarrow (\mathbb{R}^{(d+2) \times (d+2)})^M$ is given by

$$\mathcal{Q}(\mathbf{x}, \boldsymbol{\ell}) := (\mathbf{Q}_{(n,m)} - \mathbf{I}_{d+2})_{(n,m) \in E},$$

and the positive semi-definite constraint is encoded in

$$\mathcal{G}(\mathbf{U}) := \sum_{(n,m) \in E} \iota_{\mathcal{C}}(\mathbf{U}_{(n,m)}),$$

where $\iota_{\mathcal{C}}$ denotes the *indicator function* that is 0 on \mathcal{C} and $+\infty$ otherwise, and where

$$\mathcal{C} := \{\mathbf{A} \in \mathbb{R}^{(d+2) \times (d+2)} : \mathbf{A} = \mathbf{A}^T, \mathbf{A} \succeq -\mathbf{I}_{d+2}\}.$$

For (22) and $\rho > 0$, ADMM reads as

$$(\mathbf{x}^{(k+1)}, \boldsymbol{\ell}^{(k+1)}) := \arg \min_{\mathbf{x} \in (\mathbb{R}^d)^N, \boldsymbol{\ell} \in \mathbb{R}^M} \mathcal{K}(\mathbf{x}, \boldsymbol{\ell}) + \frac{\rho}{2} \|\mathcal{Q}(\mathbf{x}, \boldsymbol{\ell}) - \mathbf{U}^{(k)} + \mathbf{Z}^{(k)}\|^2, \quad (23)$$

$$\mathbf{U}^{(k+1)} := \arg \min_{\mathbf{U} \in (\mathbb{R}^{(d+2) \times (d+2)})^M} \mathcal{G}(\mathbf{U}) + \frac{\rho}{2} \|\mathcal{Q}(\mathbf{x}^{(k+1)}, \boldsymbol{\ell}^{(k+1)}) - \mathbf{U} + \mathbf{Z}^{(k)}\|^2, \quad (24)$$

$$\mathbf{Z}^{(k+1)} := \mathbf{Z}^{(k)} + \mathcal{Q}(\mathbf{x}^{(k+1)}, \boldsymbol{\ell}^{(k+1)}) - \mathbf{U}^{(k+1)},$$

where $\|\mathbf{U}\|^2 := \sum_{(n,m) \in E} \|\mathbf{U}_{(n,m)}\|_{\mathbb{F}}^2$ and $\|\cdot\|_{\mathbb{F}}$ denotes the *Frobenius norm*, see also [13]. Note that we could alternatively define \mathcal{Q} as a mapping to the linear subspace of symmetric matrices in $\mathbb{R}^{(d+2) \times (d+2)}$. It remains to give explicit formulas for the first and second update step.

Theorem 12. For $\rho > 0$, the solution of (23) is given by

$$\begin{aligned} \mathbf{x}_n^{(k+1)} &= \frac{1}{2\nu_n} \left((\mathcal{Q}_{\mathbf{x}}^*(\mathbf{U}^{(k)} - \mathbf{Z}^{(k)}))_n + \frac{1}{\rho} w_n \mathbf{y}_n \right), \\ \boldsymbol{\ell}_{(n,m)}^{(k+1)} &= \frac{1}{2} \left((\mathcal{Q}_{\boldsymbol{\ell}}^*(\mathbf{U}^{(k)} - \mathbf{Z}^{(k)}))_{(n,m)} + \frac{1}{\rho} \lambda_{(n,m)} \right), \end{aligned}$$

where $\nu_n := |\{(n,m) \in E\}| + |\{(m,n) \in E\}|$ counts the edges starting or ending in n , and the restrictions $\mathcal{Q}_{\mathbf{x}}^* := \mathcal{Q}^*|_{(\mathbb{R}^d)^N}$ and $\mathcal{Q}_{\boldsymbol{\ell}}^* := \mathcal{Q}^*|_{\mathbb{R}^M}$ of the adjoint operator \mathcal{Q}^* with respect to the component spaces are given for $n \in V$ and $i = 1, \dots, d$ by

$$((\mathcal{Q}_{\mathbf{x}}^*(\mathbf{U}))_n)_i = \left[\sum_{(n,m) \in E} (\mathbf{U}_{(n,m)})_{i,d+1} + (\mathbf{U}_{(n,m)})_{d+1,i} \right] + \left[\sum_{(m,n) \in E} (\mathbf{U}_{(n,m)})_{i,d+2} + (\mathbf{U}_{(n,m)})_{d+2,i} \right]$$

and for $(n,m) \in E$ by

$$(\mathcal{Q}_{\boldsymbol{\ell}}^*(\mathbf{U}))_{(n,m)} = (\mathbf{U}_{(n,m)})_{d+1,d+2} + (\mathbf{U}_{(n,m)})_{d+2,d+1}.$$

Proof. Setting the gradient with respect to \mathbf{x} and $\boldsymbol{\ell}$ of the objective in (23) to zero, we obtain

$$\begin{aligned}\frac{1}{\rho}(w_n \mathbf{y}_n)_{n \in V} + \mathcal{Q}_{\mathbf{x}}^*(\mathbf{U}^{(k)} - \mathbf{Z}^{(k)}) &= \mathcal{Q}_{\mathbf{x}}^*(\mathcal{Q}(\mathbf{x}, \boldsymbol{\ell})), \\ \frac{1}{\rho}\lambda + \mathcal{Q}_{\boldsymbol{\ell}}^*(\mathbf{U}^{(k)} - \mathbf{Z}^{(k)}) &= \mathcal{Q}_{\boldsymbol{\ell}}^*(\mathcal{Q}(\mathbf{x}, \boldsymbol{\ell})).\end{aligned}$$

Due to $(\mathcal{Q}_{\mathbf{x}}^*(\mathcal{Q}(\mathbf{x}, \boldsymbol{\ell})))_n = 2\nu_n \mathbf{x}_n$ and $(\mathcal{Q}_{\boldsymbol{\ell}}^*(\mathcal{Q}(\mathbf{x}, \boldsymbol{\ell})))_{(n,m)} = 2\boldsymbol{\ell}_{(n,m)}$, we obtain the assertion. \square

The second ADMM step (24) can be separately computed for single edges $(n, m) \in E$ and consists in finding $\mathbf{U}_{(n,m)}$

$$\arg \min_{\mathbf{U}_{(n,m)} \in \mathbb{R}^{(d+2) \times (d+2)}} \iota_{\mathcal{C}}(\mathbf{U}_{(n,m)}) + \frac{\rho}{2} \|(\mathcal{Q}(\mathbf{x}^{(k+1)}, \boldsymbol{\ell}^{(k+1)}))_{(n,m)} - \mathbf{U}_{(n,m)} + \mathbf{Z}_{(n,m)}^{(k)}\|_{\mathbb{F}}^2,$$

which is the projection of $(\mathcal{Q}(\mathbf{x}^{(k+1)}, \boldsymbol{\ell}^{(k+1)}))_{(n,m)} + \mathbf{Z}_{(n,m)}^{(k)}$ onto \mathcal{C} .

Theorem 13. Let $\mathbf{A} = \mathbf{V}\boldsymbol{\Sigma}\mathbf{V}^T \in \mathbb{R}^{(d+2) \times (d+2)}$ be symmetric with $\mathbf{V}^T\mathbf{V} = \mathbf{I}_{d+2}$ and diagonal matrix $\boldsymbol{\Sigma} \in \mathbb{R}^{(d+2) \times (d+2)}$. Then it holds

$$\text{proj}_{\mathcal{C}}(\mathbf{A}) = \mathbf{V}\hat{\boldsymbol{\Sigma}}\mathbf{V}^T,$$

where $\hat{\boldsymbol{\Sigma}} := \max(\text{diag}(\boldsymbol{\Sigma}), -1)$ is meant componentwise.

Proof. For any $\hat{\mathbf{A}} \in \mathcal{C}$, we have

$$\|\hat{\mathbf{A}} - \mathbf{A}\|_{\mathbb{F}} = \|\underbrace{\mathbf{V}^T \hat{\mathbf{A}} \mathbf{V}}_{=: \mathbf{B}} - \boldsymbol{\Sigma}\|_{\mathbb{F}}.$$

Since $\hat{\mathbf{A}} \succeq -\mathbf{I}_{d+2}$, we know that $\mathbf{B}_{ii} \geq -1$. Hence we obtain

$$\|\hat{\mathbf{A}} - \mathbf{A}\|_{\mathbb{F}}^2 \geq \sum_{i=1}^{d+2} |\mathbf{B}_{ii} - \boldsymbol{\Sigma}_{ii}|^2 \geq \sum_{i \in \{i: \boldsymbol{\Sigma}_{ii} < -1\}} |\mathbf{B}_{ii} - \boldsymbol{\Sigma}_{ii}|^2 \geq \sum_{i \in \{i: \boldsymbol{\Sigma}_{ii} < -1\}} |\boldsymbol{\Sigma}_{ii} + 1|^2.$$

Now the lower bound is exactly attained for $\hat{\mathbf{A}} = \mathbf{V}\hat{\boldsymbol{\Sigma}}\mathbf{V}^T$ with $\hat{\boldsymbol{\Sigma}} = \max(\text{diag}(\boldsymbol{\Sigma}), -1)$. \square

Note that the special structure of $\mathbf{Q}_{(n,m)} - \mathbf{I}_{d+2}$ is not preserved by the projection onto \mathcal{C} . Summarizing the update steps in Theorem 12 and 13, we can solve our simplified relaxed real model (15) using the following ADMM scheme, whose convergence is here ensured by [6, Cor 28.3].

Algorithm 14 (ADMM for Solving (15)).

Input: $\mathbf{y} \in (\mathbb{R}^d)^N$, $w \in \mathbb{R}_+^N$, $\lambda \in \mathbb{R}_+^M$, $\rho > 0$.

Initiation: $\mathbf{x}^{(0)} \leftarrow 0 \in (\mathbb{R}^d)^N$, $\boldsymbol{\ell}^{(0)} \leftarrow 0 \in \mathbb{R}^M$,

$\mathbf{U}^{(0)} \leftarrow \mathbf{Z}^{(0)} \leftarrow 0 \in (\mathbb{R}^{(d+2) \times (d+2)})^M$,

Iteration: For $k = 0, 1, 2, 3, \dots$ until convergence:

$$\mathbf{x}_n^{(k+1)} \leftarrow \frac{1}{2\nu_n} ((\mathcal{Q}_{\mathbf{x}}^*(\mathbf{U}^{(k)} - \mathbf{Z}^{(k)}))_n + \frac{1}{\rho} w_n \mathbf{y}_n) \text{ for all } n \in V \text{ (see Thm 12).}$$

$$\boldsymbol{\ell}_{(n,m)}^{(k+1)} \leftarrow \frac{1}{2} ((\mathcal{Q}_{\boldsymbol{\ell}}^*(\mathbf{U}^{(k)} - \mathbf{Z}^{(k)}))_{(n,m)} + \frac{1}{\rho} \lambda_{(n,m)}) \text{ for all } (n, m) \in E \text{ (see Thm 12).}$$

$$\mathbf{U}_{(n,m)}^{(k+1)} \leftarrow \text{proj}_{\mathcal{C}}((\mathcal{Q}(\mathbf{x}^{(k+1)}, \boldsymbol{\ell}^{(k+1)}))_{(n,m)} + \mathbf{Z}_{(n,m)}^{(k)}) \text{ for all } (n, m) \in E \text{ (see Thm 13).}$$

$$\mathbf{Z}^{(k+1)} \leftarrow \mathbf{Z}^{(k)} + \mathcal{Q}(\mathbf{x}^{(k+1)}, \boldsymbol{\ell}^{(k+1)}) - \mathbf{U}^{(k+1)}.$$

Output: $(\tilde{\mathbf{x}}, \tilde{\boldsymbol{\ell}})$ solving (15).

Similar schemes can be derived for the relaxed complex and quaternion problem.

	mean	time	iter.
PMM on (5)	10^{-9}	2.10	201
ADMM on (10)	10^{-12}	1.83	182
ADMM on (11)	10^{-13}	1.77	181

Table 1: The mean distance to the circle, computation time, and iteration numbers for the line graph signal in Section 6.1 with $\kappa = 10$. The recorded values are averages over 50 randomly generated ground truths.

6 Numerical Experiments

During the following numerical simulation, we give a proof-of-the-concept for denoising sphere and $\text{SO}(3)$ -valued data. We compare our simplified relaxed real model (11) with Condat’s relaxed complex model (5) for circle-valued data. Here, the proposed ADMM in Algorithm 14 shows a significant faster convergence behaviour than the originally proposed *Proximal Method of Multipliers* (PMM) in [16], which depends on two parameters τ and σ . Furthermore, we apply our simplified relaxed real method for hue and chromaticity denoising in imaging. The employed algorithms are implemented¹ in Python 3.11.4 using Numpy 1.25.0 and Scipy 1.11.1. The experiments are performed on an off-the-shelf iMac 2020 with Apple M1 Chip (8-Core CPU, 3.2 GHz) and 8 GB RAM.

6.1 \mathbb{S}_1 -Valued Data

We start with a synthetic, smooth signal $(\mathbf{x}_n)_{n \in V}$ on the line graph. More precisely, we consider the circle-valued, one-dimensional signal in Figure 1. The synthetic noisy observation $(\mathbf{y}_n)_{n \in V}$ are generated using the *von Mises–Fisher* distribution by

$$\mathbf{y}_n \sim \mathcal{N}_{\text{VMF}}(\mathbf{x}_n, \kappa) \quad \text{for all } n \in V,$$

where $\kappa > 0$ is the so-called capacity. To denoise the generated measurements, we apply PMM ($\tau := 0.1$, $\sigma := (4\tau)^{-1}$) on the relaxed complex model (5), ADMM ($\rho := 3$) on the relaxed real model (10), and compare these with ADMM ($\rho := 3$) in Algorithm 14 for the simplified relaxed real model (11), where the regularization parameters are chosen as $w_n := 1$ and $\lambda_{(n,m)} := 25$. Starting all algorithms from zero, we observe convergence to the same limit, which is shown in Figure 1.

Additionally, we compare the numerical solution of the relaxed models with the one of the TV solver CPPA-TV (cyclic proximal point algorithm for TV of circle-valued data) from [10]. Since the underlying signal is rather smooth, we observe the well-known staircase effects of the TV regularization. For this comparison, we stop both algorithm—ADMM on (11) and CPPA-TV—if the residuum (the difference between subsequent iterates in the 2-norm) is smaller than 10^{-4} . Although our method has to handle positive semi-definite matrices, the computation time amounts to 3 seconds, whereas CPPA-TV, which solves the TV regularization directly on the circle, needs 25 seconds. To compare the convergence speed with respect to the three different relaxed Tikhonov models in more detail, we run those algorithms in a second experiment for 600 iterations and determine the time after which the objective remains in a small $\epsilon := 10^{-5}$ neighbourhood around the limiting value. These times are recorded in Table 1. For the relaxed complex model (5), ADMM shows a significant speed-up compared with PMM. Moreover, switching to our simplified relaxed real model gives an additional acceleration. Notice that the solution $(\tilde{\mathbf{x}}_n)_{n \in V}$ of (11) fulfils $\|\tilde{\mathbf{x}}_n\| \leq 1$, since $\mathbf{Q}_{(n,m)} \succeq 0$ and thus

$$\det \begin{pmatrix} \mathbf{I} & \tilde{\mathbf{x}}_n \\ \tilde{\mathbf{x}}_n^\top & 1 \end{pmatrix} = 1 - \|\tilde{\mathbf{x}}_n\|^2 \geq 0$$

for all $(n, m) \in E$. For the relaxed complex models, there holds an analogous observation. Determining the mean of $1 - \|\tilde{\mathbf{x}}_n\|$ over $n \in V$ as well as of $1 - |x_n|$ for the numerical real and complex solutions, see Table 1, we observe convergence to the circle, i.e. the numerical solutions solve the original (unrelaxed) problem (6). For the simulation in Figure 1, the mean distance to the circle over the run time is reported in Figure 2.

¹The code is available at GitHub: https://github.com/JJEWBresch/relaxed_tikhonov_regularization.

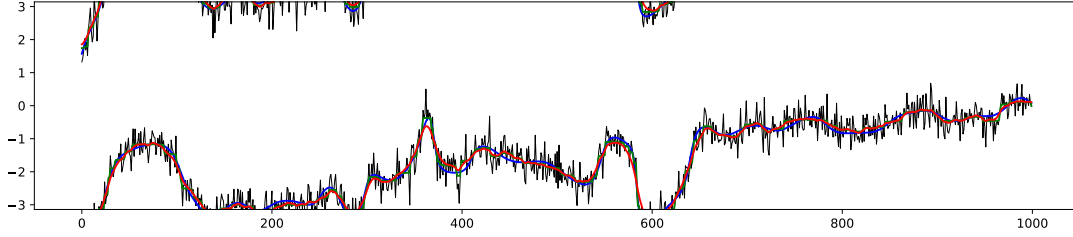


Figure 1: Ground truth (blue), noisy observation with $\kappa = 10$ (black), numerical solution by Alg. 14 (red) with $\lambda \equiv 25$ and $\rho = 3$ of the line graph signal of length $N = 1000$ in Section 6.1 in comparison with the solution obtained by CPPA-TV (green) with regularization parameter $\lambda \equiv 0.8$ and $\lambda_0 = \pi$. The \mathbb{S}_1 -values are represented by their angles in $[-\pi, \pi)$.

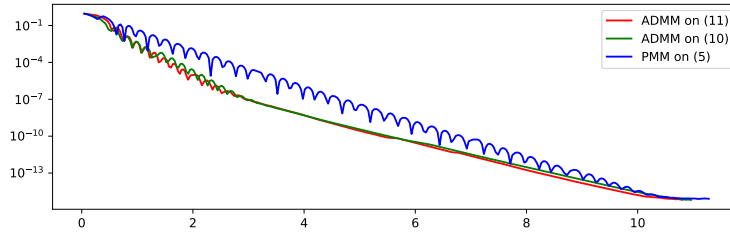


Figure 2: Mean distance to the circle over the computation time for the experiment in Figure 1.

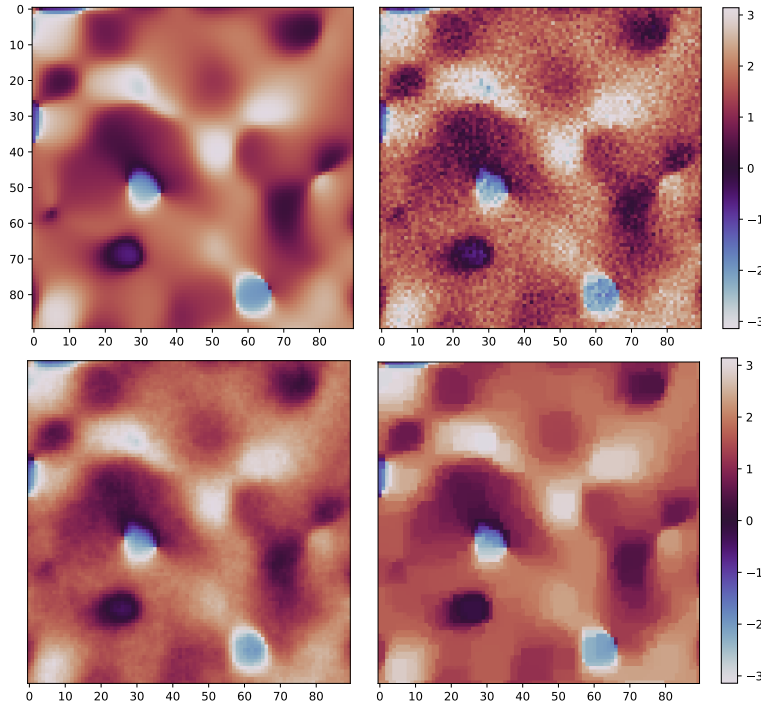


Figure 3: *Top row:* Ground truth (left) and noisy observation with $\kappa = 20$ (right). *Bottom row:* Numerical solution (left) using Alg. 14 on the 90×90 pixel image graph signal in Section 6.1 with $w_n \equiv 1$, $\lambda \equiv 1$ and $\rho = 3$. The solution comes with an restoration error (RMSE) $7.627 \cdot 10^{-2}$, mean distance to the sphere $7.834 \cdot 10^{-5}$. Comparison with CPPA-TV (right) with $\lambda \equiv 0.3$ and $\lambda_0 = \pi$. The solution comes with an restoration error (RMSE) $8.702 \cdot 10^{-2}$. The colour map corresponds to the angles of the \mathbb{S}_1 -values.

	mean	time	iter.
PMM on (5)	10^{-4}	747.18	5536
ADMM on (10)	10^{-4}	389.01	2457
ADMM on (11)	10^{-4}	301.08	1943

Table 2: The mean distance to the circle, computation time, and iteration numbers for the image graph signal in Section 6.1 with $\kappa = 20$. The recorded values are averages over 50 randomly generated ground truths.

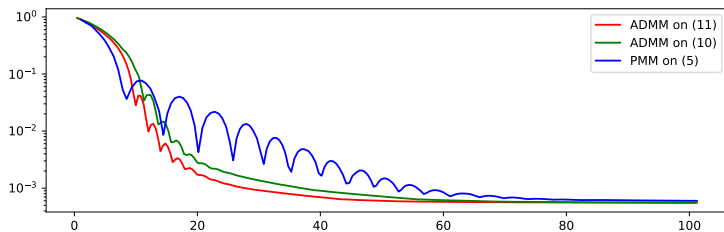


Figure 4: Mean distance to the circle over the computation time for the experiment in Figure 1.

For \mathbb{S}_1 -valued images, the (*image*) graph G consists of the image pixels, which are connected to their vertical and horizontal neighbours. As before, we generate synthetic observation using the von Mises–Fisher distribution. The synthetic observations are denoised using PMM ($\tau := 0.1$, $\sigma := (8\tau)^{-1}$) on the relaxed complex model (5), ADMM ($\rho := 3$) on the relaxed real model (10), as well as ADMM ($\rho := 3$) on the simplified relaxed real model (11), where the regularization parameters are chosen as $w_n := 1$ and $\lambda_{(n,m)} := 1$. The generated data together with its denoised version, which nearly coincides for all three methods, are shown in Figure 3. Similarly to the previous example, we compare our relaxed models with CPPA-TV. The typical staircase effects can again be observed together with a larger restoration error (root mean squared error (RMSE)) compared to our model. The stopping criteria is chosen as for the line-graph example above. The computation time for our approach amounts to 65 seconds and for CPPA-TV to 367 seconds. To compare the convergence speed with respect to the three different relaxed Tikhonov models in more details, we run the algorithms in a second experiment for 6000 iterations and determine the time after which the objective stays in an $\epsilon := 10^{-3}$ neighborhood around the limiting value. These times are recorded in Table 2. Differently from the line-graph setting, all methods show much slower numerical convergence. Similarly, the convergence of \mathbf{x}_n to \mathbb{S}_1 and x_n to $\mathbb{S}_{\mathbb{C}}$ is slowed down but can be observed after the final iteration, see Figure 4. This behaviour has also been observed in [16] and transfers to our simplified relaxed real model. It seems that this drawback only occurs for circle-valued images. The benefit of ADMM and our simplified relaxed real model with respect to the computation time are clearly visible.

6.2 Denoising Colour Values

Sphere-valued data naturally occur as colour information of colour images. For instance, the hue of the HSV (hue, saturation, value) colour model is \mathbb{S}_1 -valued, and the chromaticity of the CB (chromaticity, brightness) colour model is \mathbb{S}_2 -valued, see [15, § 1.1]. Identifying the circle $\mathbb{S}_1 = \{(\cos \alpha, \sin \alpha)^T : \alpha \in [0, 2\pi)\}$ with the angle $\alpha \in [0, 2\pi)$, the hue starts with red at 0, goes over green at $2\pi/3$ and blue at $4\pi/3$, and return to red at 2π . The chromaticity is the normalized colour vector of the RGB (red, green, blue) model. For the numerical simulations, we take the hue and the chromaticity of the colour image in Figure 5, perturb the colour values according to the von Mises–Fisher distribution, and apply Algorithm 14 based on the simplified real model for denoising. The results are shown in Figure 5 and 6. Visually, most of the noise is removed.

6.3 $\text{SO}(3)$ -Valued Data

As discussed in Section 4, we want to employ Algorithm 14 to denoise 3d rotation data on line and image graphs. Starting from a smooth $\text{SO}(3)$ -valued signal $(\mathbf{R}_n)_{n \in V}$ corresponding to the rotation axes $\mathbf{v}_n \in \mathbb{S}_2$ and rotation angles $\alpha_n \in \mathbb{S}_1$, i.e. $\mathbf{R}_n = \mathbf{R}(\mathbf{v}_n, \alpha_n)$, we generate disturbed rotation axes and angles with respect to the von Mises–Fisher distributions on \mathbb{S}_2 and \mathbb{S}_1 . More precisely, we sample

$$\mathbf{w}_n \sim \mathcal{N}_{\text{VMF}}(\mathbf{v}_n, \kappa_1) \quad \text{and} \quad \beta_n \sim \mathcal{N}_{\text{VMF}}(\alpha_n, \kappa_2).$$

The synthetic observations are then given by $(\mathbf{S}_n)_{n \in V}$ with $\mathbf{S}_n := \mathbf{R}(\mathbf{w}_n, \beta_n)$. The aim is now to denoise the signal $(\mathbf{S}_n)_{n \in V}$. For this, we use the double cover $\text{SO}(3) \cong \mathbb{S}_{\mathbb{H}}/\{-1, 1\}$ to represent the 3×3 matrices \mathbf{S}_n by their quaternion $q_n := \pm q(\mathbf{w}_n, \beta_n)$, see (16). Starting with $q_1 := q(\mathbf{w}_1, \beta_1)$ the remaining signs of q_n are here chosen such that $\Re[q_n q_m] \geq 0$ for all $(n, m) \in E$. In this example, the original signal

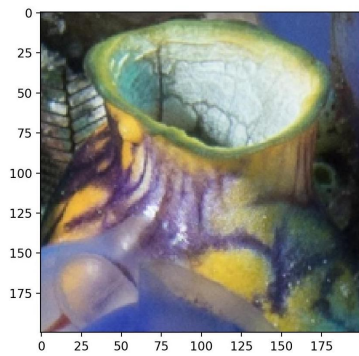


Figure 5: *Left:* Ground truth of size 200×200 for the colour denoising in Section 6.2.

Below: Hue ground truth (left), noisy observation with $\kappa = 10$ (middle), and denoised version (right) of the hue experiment in Section 6.2 with respect to Figure 5. ADMM has been employed with $w_n := 1$, $\lambda_{(n,m)} := 1$ and $\rho := 3$. The solution comes with an mean distance to the sphere $5.874 \cdot 10^{-4}$.

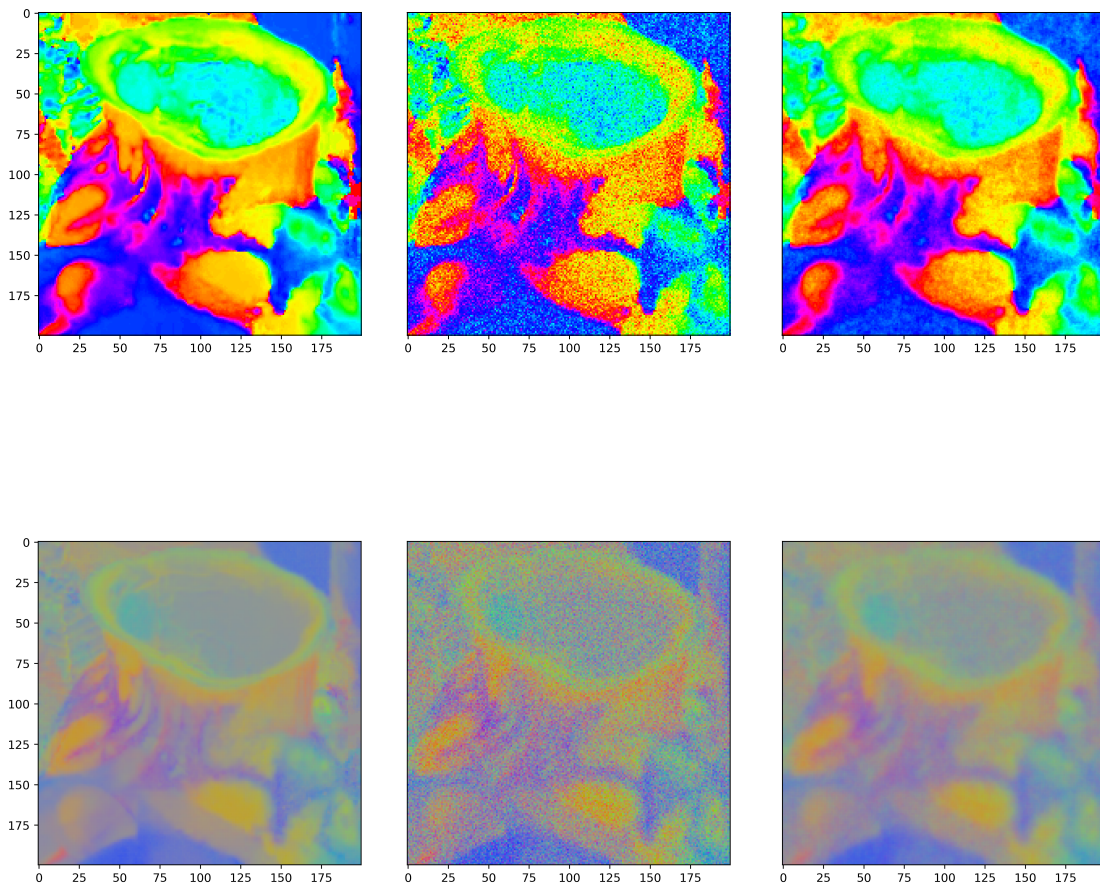


Figure 6: Ground truth (left), noisy observation with $\kappa = 100$ (middle), and denoised version (right) of the chromaticity experiment in Section 6.2 with respect to Figure 5. ADMM has been employed with $w_n := 1$, $\lambda_{(n,m)} := 3$, and $\rho := 3$. The solution comes with an mean distance to the sphere $2.343 \cdot 10^{-10}$.

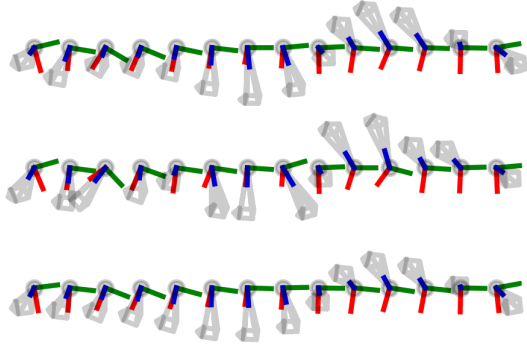


Figure 7: Ground truth (top), noisy observation with $\kappa_1 := 30$ and $\kappa_2 := 15$ (middle), and denoised version (bottom) of the $\text{SO}(3)$ -valued signal on the line graph in Section 6.3. The rotations are visualized by operating on a 3d object. The red, green, and blue lines indicate the rotated unit vectors. The entire signal has a length of $N := 1000$, where only the rotations at $n = 1, 11, 21, 31, \dots$ are visualized. The parameters have been $w_n := 1$, $\lambda_{(n,m)} := 50$, and $\rho := 3$. The solution comes with an mean distance to the unit quaternions $3.245 \cdot 10^{-12}$.

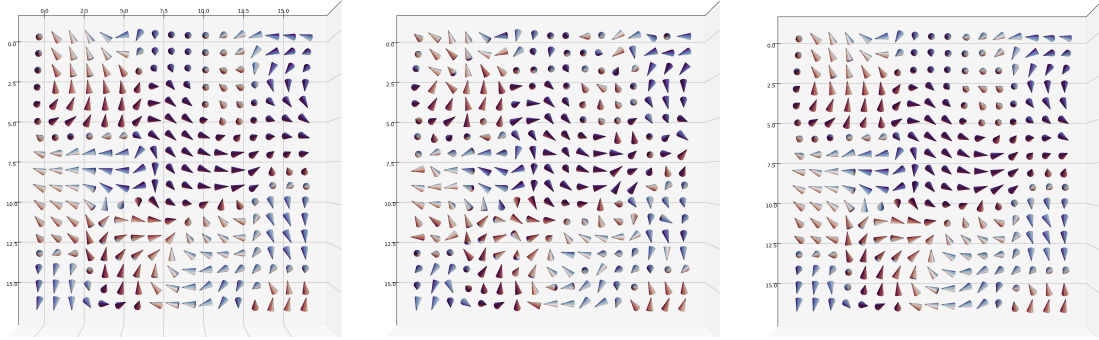


Figure 8: Ground truth (left), noisy observation with $\kappa_1 := 30$ and $\kappa_2 := 5$ (middle), and denoised version (right) of the $\text{SO}(3)$ -valued signal on the image graph in Section 6.3. The rotations are visualized by operating on a colored 3d cone. The entire signal consists of 90×90 pixel, where only every third pixel from the 25th to the 75th pixel is visualized. The parameters have been $w_n := 1$, $\lambda_{(n,m)} := 1$, and $\rho := 3$. The solution comes with an mean distance to the unit quaternions $1.667 \cdot 10^{-10}$.

is smooth and the noise small enough such that the sign choice is well defined. Finally, Algorithm 14 is employed on the vector representations $\mathbf{q}_n := (\Re[q_n], \Im_i[q_n], \Im_j[q_n], \Im_k[q_n])^T$. For the line graph, see Figure 7, ADMM takes 8.60 seconds (209 iterations) to converge. For the image graph, see Figure 8, ADMM needs 41.69 seconds (219 iterations) until convergence. In both cases, the mean of $1 - \|\mathbf{q}_n\|$ over $n \in V$ reaches 10^{-9} after around 200 iterations. Hence, the computed numerical solutions are in fact solutions of the original unrelaxed problem.

Appendix

Proof of Theorem 9. Recall the identification of the quaternion $z \in \mathbb{H}$ with $\mathbf{z} := (\Re[z], \Im_i[z], \Im_j[z], \Im_k[z]) \in \mathbb{R}^4$ such that $|z| = \|\mathbf{z}\|$. Moreover, each quaternion can be identified with the matrix

$$\mathbf{M}(z) := \begin{bmatrix} \Re[z] & -\Im_i[z] & -\Im_j[z] & -\Im_k[z] \\ \Im_i[z] & \Re[z] & -\Im_k[z] & \Im_j[z] \\ \Im_j[z] & \Im_k[z] & \Re[z] & -\Im_i[z] \\ \Im_k[z] & -\Im_j[z] & \Im_i[z] & \Re[z] \end{bmatrix} \in \mathbb{R}^{4 \times 4}.$$

In this way, the addition and multiplication of quaternions carries over to the addition and multiplication of the associated matrices. The matrix $P_{(n,m)} \in \mathbb{H}^{3 \times 3}$ in (18) is positive semi-definite if and only if the

real-valued representation

$$\mathbf{P}_{(n,m)} := \begin{bmatrix} \mathbf{I}_4 & \mathbf{M}(\mathbf{x}_n) & \mathbf{M}(\mathbf{x}_m) \\ \mathbf{M}(\mathbf{x}_n)^\top & \mathbf{I}_4 & \mathbf{M}(\mathbf{r}_{(n,m)})^\top \\ \mathbf{M}(\mathbf{x}_m)^\top & \mathbf{M}(\mathbf{r}_{(n,m)}) & \mathbf{I}_4 \end{bmatrix} \in \mathbb{R}^{12 \times 12}$$

is positive semi-definite. In order to establish the equality between quaternion model (19) and the real-valued model in (15) for $d = 4$, we compare the Schur complements of a permuted version of $\mathbf{P}_{(n,m)}$ and of $\mathbf{Q}_{(n,m)}$. First, we compute the Schur complement of $\mathbf{Q}_{m,n}$ in (21) with respect to \mathbf{I}_4 , which is again given by

$$\mathbf{Q}_{(n,m)}/\mathbf{I}_4 = \begin{bmatrix} 1-|\mathbf{x}_n|^2 & \ell_{(n,m)} - \langle \mathbf{x}_n, \mathbf{x}_m \rangle \\ \ell_{(n,m)} - \langle \mathbf{x}_n, \mathbf{x}_m \rangle & 1-|\mathbf{x}_m|^2 \end{bmatrix}.$$

Second, we consider the matrix $\mathbf{P}_{(n,m)}$ whose details are given in Table 3a. Permuting the columns and rows of $\mathbf{P}_{(n,m)}$ with respect to the permutation (1, 2, 3, 4, 5, 9, 6, 10, 7, 11, 8, 12), we obtain $\tilde{\mathbf{P}}_{(n,m)}$ in Table 3b. Forming the Schur complement with respect to the upper left identity results in the block matrix $\tilde{\mathbf{P}}_{(n,m)}/\mathbf{I}_4$ in Table 3c.

Comparing the Schur complements $\mathbf{Q}_{(n,m)}/\mathbf{I}_4$ and $\tilde{\mathbf{P}}_{(n,m)}/\mathbf{I}_4$ and using $\Re[\bar{x}_m x_n] = \langle \mathbf{x}_m, \mathbf{x}_n \rangle$, we obtain the following: if (\hat{x}, \hat{r}) solves (19), then $(\hat{\mathbf{x}}, \hat{\boldsymbol{\ell}})$ with $\hat{\boldsymbol{\ell}}_{(n,m)} := \Re[\hat{r}_{(n,m)}]$ is a feasible point of (15). Moreover, it holds $\mathcal{K}(\hat{\mathbf{x}}, \hat{\boldsymbol{\ell}}) = \mathcal{J}(\hat{x}, \hat{r})$. Conversely, if $(\tilde{\mathbf{x}}, \tilde{\boldsymbol{\ell}})$ solves (15), then (\tilde{x}, \tilde{r}) with \tilde{r} defined in the assertion is a feasible point of (19)—all off-diagonal blocks of $\tilde{\mathbf{P}}_{(n,m)}/\mathbf{I}_4$ become zero—and again $\mathcal{K}(\tilde{\mathbf{x}}, \tilde{\boldsymbol{\ell}}) = \mathcal{J}(\tilde{x}, \tilde{r})$. Then, taking the minimizing property into account, we conclude

$$\mathcal{K}(\tilde{\mathbf{x}}, \tilde{\boldsymbol{\ell}}) \leq \mathcal{K}(\hat{\mathbf{x}}, \hat{\boldsymbol{\ell}}) = \mathcal{J}(\hat{x}, \hat{r}) \leq \mathcal{J}(\tilde{x}, \tilde{r}) = \mathcal{K}(\tilde{\mathbf{x}}, \tilde{\boldsymbol{\ell}})$$

which is only possible if all values coincides. This yields the assertion. \square

Acknowledgements

Funding by the DFG excellence cluster MATH+ and by the BMBF project “VI-Screen” (13N15754) are gratefully acknowledged. Many thanks to L. Condat for discussions on the topic.

References

- [1] B. L. Adams, S. I. Wright, and K. Kunze. Orientation imaging: the emergence of a new microscopy. *Metall. Mater. Trans. A Phys. Metall. Mater. Sci.*, 24:819–831, 1993.
- [2] M. Bačák, R. Bergmann, G. Steidl, and A. Weinmann. A second order non-smooth variational model for restoring manifold-valued images. *SIAM J. Sci. Comput.*, 38(1):A567–A597, 2016.
- [3] F. Bachmann, R. Hielscher, P. E. Jupp, W. Pantleon, H. Schaeben, and E. Wegert. Inferential statistics of electron backscatter diffraction data from within individual crystalline grains. *J. Appl. Crystallogr.*, 43:1338–1355, 2010.
- [4] F. Bachmann, R. Hielscher, and H. Schaeben. Grain detection from 2d and 3d EBSD data—specification of the MTEX algorithm. *Ultramicroscopy*, 111(12):1720–1733, 2011.
- [5] T. Batard and M. Bertalmio. A geometric model of brightness perception and its application to color image correction. *J. Math. Imaging Vis.*, 60(6):849–881, 2018.
- [6] H. H. Bauschke and P. L. Combettes. *Convex analysis and monotone operator theory in Hilbert spaces*. CMS Books in Mathematics/Ouvrages de Mathématiques de la SMC. Springer, New York, 2011.
- [7] R. Beinert and J. Bresch. Denoising sphere-valued data by relaxed total variation regularization, 2024.
- [8] R. Bergmann, R. H. Chan, R. Hielscher, J. Persch, and G. Steidl. Restoration of manifold-valued images by half-quadratic minimization. *Inverse Probl. Imaging*, 10(2):281–304, 2016.

- [9] R. Bergmann, F. Laus, J. Persch, and G. Steidl. Recent advances in denoising of manifold-valued images. In R. Kimmel and X.-C. Tai, editors, *Handbook of Numerical Analysis*, volume 20, pages 553–578. Elsevier, 2019.
- [10] R. Bergmann, F. Laus, G. Steidl, and A. Weinmann. Second order differences of cyclic data and applications in variational denoising. *SIAM J. Imaging Sci.*, 7(4):2916–2953, 2014.
- [11] S. Boyd, N. Parikh, E. Chu, B. Peleato, and J. Eckstein. Distributed optimization and statistical learning via the alternating direction method of multipliers. *Found. Trends Mach. Learn.*, 3(1):1–122, 2010.
- [12] G. E. Bredon. *Topology and Geometry*. Number 139 in Graduate Texts in Mathematics. Springer, New York, 1993.
- [13] M. Burger, A. Sawatzky, and G. Steidl. First order algorithms in variational image processing. In R. Glowinski, S. Osher, and W. Yin, editors, *Splitting methods in communication, imaging, science, and engineering*, Sci. Comput., pages 345–407. Springer, Cham, 2017.
- [14] R. Bürgmann, P. A. Rosen, and E. J. Fielding. Synthetic aperture radar interferometry to measure earth’s surface topography and its deformation. *Annu. Rev. Earth Planet Sci.*, 28(1):169–209, 2000.
- [15] T. Chan, S. Kang, and J. Shen. Total variation denoising and enhancement of color images based on the CB and HSV color models. *J. Vis. Commun. Image Represent.*, 12(4):422–435, 2001.
- [16] L. Condat. Tikhonov regularization of circle-valued signals. *IEEE Trans. Signal Process.*, 70:2775–2782, 2022.
- [17] L. Condat. Tikhonov regularization of sphere-valued signals, 2022. arxiv:2207.12330.
- [18] D. Cremers and E. Strekalovskiy. Total cyclic variation and generalizations. *J. Math. Imaging Vis.*, 47(3):258–277, 2013.
- [19] J. Cremers and I. Klugkist. One direction? A tutorial for circular data analysis using R with examples in cognitive psychology. *Front. Psychol.*, 9(2040), 2018.
- [20] C.-A. Deledalle, L. Denis, and F. Tupin. NL-InSAR: Nonlocal interferogram estimation. *IEEE Trans. Geosci. Remote Sens.*, 49(4):1441–1452, 2011.
- [21] M. Gräf. A unified approach to scattered data approximation on \mathbb{S}^3 and $\text{SO}(3)$. *Adv. Comput. Math.*, 37:379–392, 2012.
- [22] M. Gräf, S. Neumayer, R. Hielscher, G. Steidl, M. Liesegang, and T. Beck. An optical flow model in electron backscatter diffraction. *SIAM J. Imaging Sci.*, 15(1):228–260, 2022.
- [23] P. Grohs and M. Sprecher. Total variation regularization on Riemannian manifolds by iteratively reweighted minimization. *Inf. Inference*, 5(4):353–378, 2016.
- [24] R. A. Horn and C. R. Johnson. *Matrix Analysis*. Cambridge University Press, Cambridge, 2nd edition, 2012.
- [25] D. Huynh. Metrics for 3d rotations: Comparison and analysis. *SIAM J. Imaging Sci.*, 35:155–164, 10 2009.
- [26] Z. Jia, M. K. Ng, and W. Wang. Color image restoration by saturation-value total variation. *SIAM Journal on Imaging Sciences*, 12(2):972–1000, 2019.
- [27] R. Kimmel and N. Sochen. Orientation diffusion or how to comb a porcupine. *J. Vis. Commun. Image. Represent.*, 13(1):238–248, 2002.
- [28] T. Lan, D. Erdogmus, S. J. Hayflick, and J. U. Szumowski. Phase unwrapping and background correction in MRI. In *Proceedings MLSP ’08*, pages 239–243, 2008. IEEE Workshop on Machine Learning for Signal Processing, 16-19 October 2008, Cancun, Mexico.
- [29] F. Laus, M. Nikolova, J. Persch, and G. Steidl. A nonlocal denoising algorithm for manifold-valued images using second order statistics. *SIAM J. Imaging Sci.*, 10(1):416–448, 2017.

- [30] J. Lellmann, E. Strekalovskiy, S. Koetter, and D. Cremers. Total variation regularization for functions with values in a manifold. In *Proceedings ICCV '13*, pages 2944–2951, 2013. IEEE International Conference on Computer Vision, 1–8 December 2013, Sydney, Australia.
- [31] M. Nikolova and G. Steidl. Fast hue and range preserving histogram specification: theory and new algorithms for color image enhancement. *IEEE Trans. Image Process.*, 23(9):4087–4100, 2014.
- [32] N. Parikh and S. P. Boyd. Proximal algorithms. *Found. Trends Optim.*, 1:127–239, 2013.
- [33] X. Pennec. Intrinsic statistics on Riemannian manifolds: basic tools for geometric measurements. *SIAM J. Imaging Sci.*, 25:127–154, 2006.
- [34] J. Persch, F. Pierre, and G. Steidl. Exemplar-based face colorization using image morphing. *J. Imaging*, 3(4):48, 2017.
- [35] M. H. Quang, S. H. Kang, and T. M. Le. Image and video colorization using vector-valued reproducing kernel Hilbert spaces. *J. Math. Imaging Vis.*, 37:49–65, 2010.
- [36] P. A. Rosen, S. Hensley, I. R. Joughin, F. K. Li, S. N. Madsen, E. Rodriguez, and R. M. Goldstein. Synthetic aperture radar interferometry. *Proc. IEEE*, 88(3):333–382, 2000.
- [37] G. Rosman, A. M. Bronstein, M. M. Bronstein, X.-C. Tai, and R. Kimmel. Group-valued regularization for analysis of articulated motion. In *Computer Vision – ECCV '12*, pages 52–62, 2012. Workshops and Demonstrations, 7–13 October 2012, Florence, Italy.
- [38] G. Rosman, X.-C. Tai, R. Kimmel, and A. Bruckstein. Augmented-lagrangian regularization of matrix-valued maps. *Methods and Applications of Analysis*, 21:121–138, 2014.
- [39] Y. Sowa, A. D. Rowe, M. C. Leake, T. Yakushi, M. Homma, A. Ishijima, and R. M. Berry. Direct observation of steps in rotation of the bacterial flagellar motor. *Nature*, 437:916–919, 2005.
- [40] E. Strekalovskiy and D. Cremers. Total variation for cyclic structures: convex relaxation and efficient minimization. In *Proceedings CVPR '11*, pages 1905–1911, 2011. IEEE Conference on Computer Vision and Pattern Recognition, 20–25 June 2011, Colorado Springs, USA.
- [41] L. A. Vese and S. J. Osher. Numerical methods for p-harmonic flows and applications to image processing. *SIAM J. Numer. Anal.*, 40(6):2085–2104, 2002.
- [42] A. Weinmann, L. Demaret, and M. Storath. Total variation regularization for manifold-valued data. *SIAM J. Imaging Sci.*, 7(4):2226–2257, 2014.
- [43] F. Zhang. Quaternions and matrices of quaternions. *Linear Algebra Appl.*, 251:21–57, 1997.